Supplementary material for Time-optimal control of a solid-state spin amidst dynamical quantum wind

Yang Dong,[1,2] Wang Jiang,[1,2] Xue-Dong Gao,[1,2,3] Cui Yu,[3] Yong Liu,[1,2] Shao-Chun Zhang,[1,2] Xiang-Dong Chen,[1,2,4] Ibério de P. R Moreira,[5,6] Josep Maria Bofill,[5,7] Gael Sentís,[8] Ramón Ramos,[8] Guillermo Albareda,[8] Guang-Can Guo,[1,2,4] and Fang-Wen Sun[1,2,4,*]

[1]CAS Key Lab of Quantum Information,
University of Science and Technology of China, Hefei, 230026, P.R. China

[2]CAS Center For Excellence in Quantum Information and Quantum Physics,
University of Science and Technology of China, Hefei, 230026, P.R. China

[3]National Key Laboratory of Solid-State Microwave
Devices and Circuits, Shijiazhuang, 050051, P.R. China

[4]Hefei National Laboratory, University of Science
and Technology of China, Hefei 230088, P.R. China

[5]Institute of Theoretical and Computational Chemistry,
(IQTCUB), Universitat de Barcelona,
Martí i Franquès 1-11, 08028 Barcelona, Spain

[6]Departament de Ciència de Materials i Química Física,
Universitat de Barcelona, Martí i Franquès 1-11, 08028 Barcelona, Spain

[7]Departament de Química Inorgànica i Orgànica,
Secció de Química Orgànica, Universitat de Barcelona,
Carrer Martí i Franquès 1-11, 08028 Barcelona, Spain

[8]Ideaded S.L, Carrer de la Tecnologia,
35, 08840 Viladecans, Barcelona, Spain

S1. NV center in diamond

The Hamiltonian of the ^{14}NV center can be expressed as

$$H_{NV} = DS_z^2 + \gamma_e BS_z + QI_z^2 + \gamma_n BI_z + A_{zz}S_zI_z, \tag{1}$$

where D=2.87 GHz is the zero-field splitting, S_z and I_z are the electron spins, ^{14}N is the nuclear spin; γ_e, γ_n are the electronic and nuclear gyromagnetic ratio, A_{zz} is the hyperfine interaction for ^{14}N nuclear spins, and $Q = -4.95$ MHz is the quadrupole splitting of the ^{14}N nuclear spin. In the experiment, we apply a strength of the external magnetic field to be near the excited state level anti-crossing [1, 2], i.e., $B_0 = 51$ mT along the NV symmetry axis to split the energy levels and polarize intrinsic ^{14}N nuclear spin to enhance the signal contrast. The dynamics of the dark spin bath in the NV center are profoundly impacted by the strength of the applied bias magnetic field. However, for diamond sample with natural ^{13}C abundance, the dephasing time T_2^* for NV center exhibits a relatively stable behavior in response to variations in the medium magnetic field regime, except for changing with a small factor. During the experiment, the observed fluorescence signal, which is related to the population distributions between $m_s = 0$ and $m_s = \pm 1$ states of NV center, can be transformed into the probability of successful quantum coherent operation through a linear conversion [1]. To reduce photon shot noise, we repeat the experiment 5×10^8 times to reduce fluctuation (denotes with error bars) for the experimental data.

From the continuous wave optically detected magnetic resonance (CWODMR) spectrum signal, we determined that the resonant frequency of the NV center is $f_1 = 1.4309$ GHz as shown in SFig. 1a. To normalize the coherent MW operation for Ramsey signals, we conducted an electron spin nutation experiment, as shown in SFig. 1b. However, undesired couplings between the qubit and surrounding ^{13}C nuclear spins lead to the dephasing effect. The resulting Ramsey signal of the qubit is depicted in SFigure. 1c, where a dephasing time $T_2^* = 7.6$ μs is obtained. This time can be prolonged to $T_2 = 200$ μs by a single refocusing π pulse as shown in SFig. 1d. The ground state spin relaxation time of NV center is $T_1 = 1.87(2)$ ms as shown in SFig. 1e.

S2. Energy cost of the Ansatz-free approach

Given an initial state $|\psi_i\rangle$ and a timedependent drift Hamiltonian $H_0(t)$, we aim to

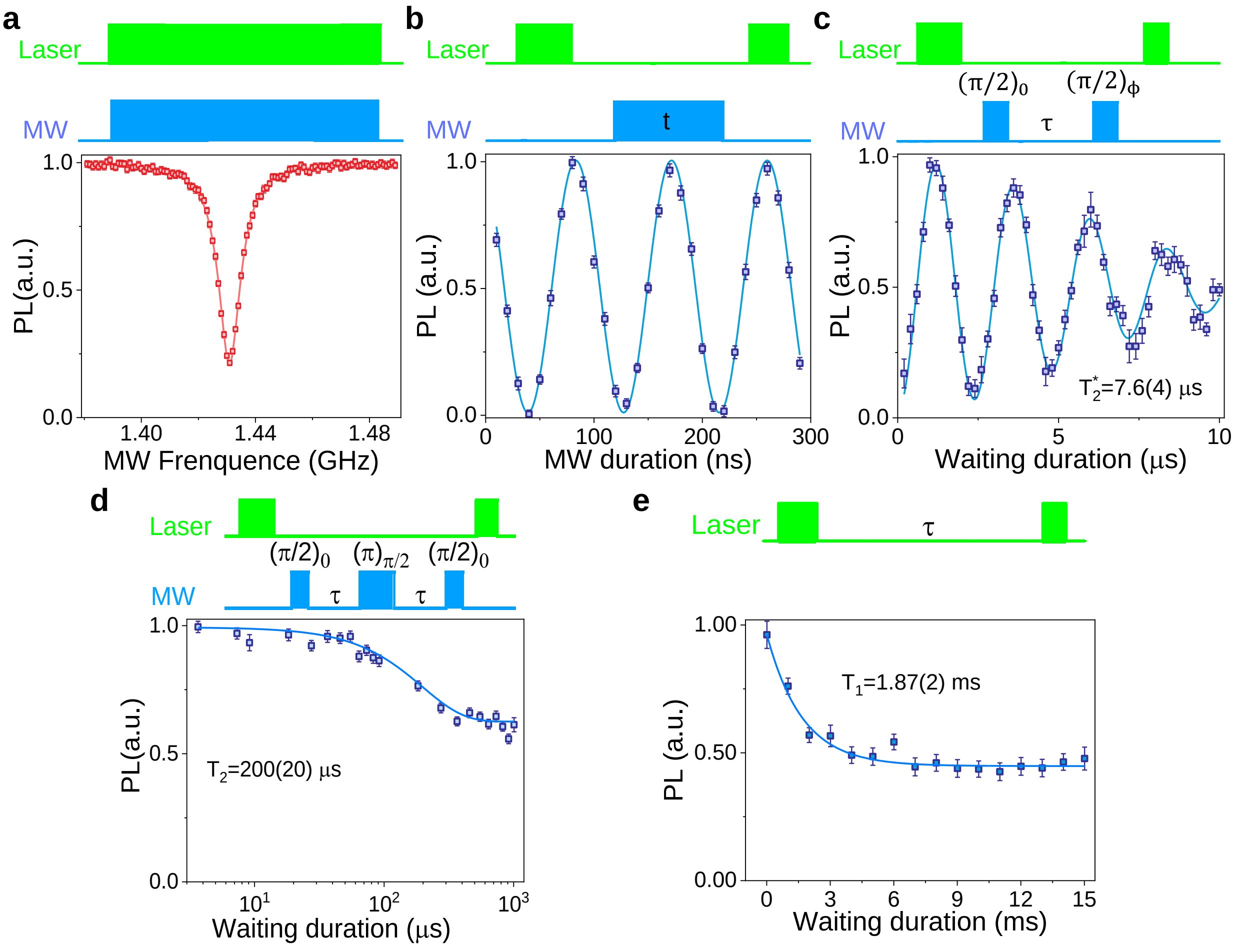

SFig. 1: **Properties of NV centers.** **a** Photoluminescence (PL) intensity of the CWODMR for the transition between the states $|m_s = 0\rangle$ and $|m_s = 1\rangle$ of the NV center. These two spin states in the NV center are encoded as qubit $|0\rangle$ and $|1\rangle$. The red curve is a fit with a single Lorentzian peak. **b** Results of the nutation experiment for the electron spin of NV center. The solid blue line in the panel is a fitting to the experimental results. The Rabi frequency is about 5.21 MHz. **c** Results of a standard Ramsey experiment on the NV center. The results (blue dots) are fitted to the function $a \exp\left[-(\tau/T_2^*)^2\right] \cos(\Delta\tau) + b$ as shown with the blue curve. The phase of the last $\pi/2$ pulse increases linearly with time ($\phi = \Delta\tau$) in the rotating frame [1]. **d-e** Coherence times (T_2, T_1) of NV center at room temperature.

find the time-optimal control Hamiltonian $H_c(t)$ such that the total Hamiltonian $H(t) = H_0(t) + H_c(t)$ drives $|\psi_i\rangle$ to the target state $|\psi_f\rangle$ in the shortest passage time τ according to the time-dependent Schrödinger equation

$$i\frac{d|\psi(t)\rangle}{dt} = H(t)|\psi(t)\rangle. \tag{2}$$

The above problem can be reformulated in the interaction picture by expressing the initial and final states as follows: $|\psi_i'\rangle = |\psi_i\rangle$ and $|\psi_f'\rangle = U_0^\dagger(\tau)|\psi_f\rangle$, where $U_0(t) = \mathcal{T}\exp\left(-i\int_0^t H_0(t_1)\,dt_1\right)$ and $\mathcal{T}$ defines the usual time ordering operator. We use the Riemannian metric [3], which in the interaction picture reads as $\mathcal{L} = 2\int_0^\tau \Delta H_c'(t)dt$, where $\Delta H_c'(t)$ denotes the standard deviation of the control Hamiltonian $H_c'(t)$. The minimum distance path between two states lies entirely in the subspace spanned by these two states is $\mathcal{L}_{\mathrm{FS}}^{\min}(i,f') = 2\arccos\left(\left|\left\langle \psi_i \mid \psi_f'\right\rangle\right|\right)$. Now, a state having evolved along a geodesic must obey $\mathcal{L} = \mathcal{L}_{FS}^{\min}(i,f')$. Furthermore, if we impose the transversality condition

$$\langle\psi'(t)\left|H_c'(t)\right|\psi'(t)\rangle = i\left\langle\psi'(t)\mid\dot{\psi}'(t)\right\rangle = 0, \tag{3}$$

we get a functional form of $H_c'(t)$, which is given by

$$H_c'(t) = i\left(\frac{d\left|\psi'(t)\right\rangle}{dt}\left\langle\psi'(t)\right| - \left|\psi'(t)\right\rangle\frac{d\left\langle\psi'(t)\right|}{dt}\right). \tag{4}$$

We express the above Hamiltonian in terms of initial and final states as

$$H_c'(t) = \frac{i\mathrm{v}_z(t)}{\sqrt{1-s^2}}\left(e^{-i\beta}\left|\psi_f'\right\rangle\left\langle\psi_i\right| - e^{i\beta}\left|\psi_i\right\rangle\left\langle\psi_f'\right|\right), \tag{5}$$

where s and β are defined through $\left\langle\psi_i' \mid \psi_f'(\tau)\right\rangle = se^{i\beta}$. Given H_c', we can already propagate the initial state $|\psi_i\rangle$ according to the time-dependent Schrödinger equation, where $H = H_0(t) + H_c(t)$ and $H_c(t) = U_0 H_c'(t) U_0^\dagger$.

The energy cost of the optimal control field can be expressed generally as follows:

$$E_2(\tau) = k_2\int_0^\tau \|H_c(t)\|^2 dt, \tag{6}$$

where k_2 is a setup dependent constant. To determine the parameter value of $k_"$, we conducted measurements of the oscillation frequencies with different input MW powers (P), as depicted in SFig. 2. The figure plots the Rabi oscillation frequencies as a function of the square root of the input MW power. The observed data can be fitted by a linear function fixing the intercept at zero, and hence we get $k_2 = c^2 = \left(3.40(1)\frac{MHz}{\sqrt{W}}\right)^{-2}$.

S3. Hamiltonian engineering with a NV center

By tuning the MW frequency resonant with the $m_s = 0 \leftrightarrow m_s = +1$ transition as shown

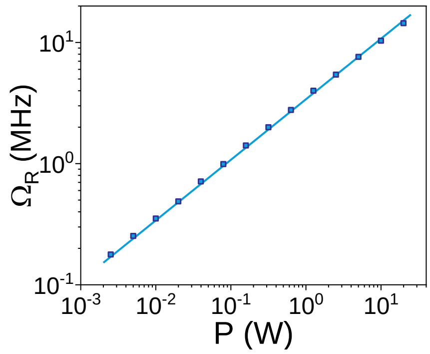

SFig. 2: **The relationship between Rabi frequency and MW power.** Dependence of the effective Rabi frequency Ω_R on the square root of the MW power fed to the planar MW antenna for the transition $|m_s = 0\rangle$ and $|m_s = 1\rangle$. The results (blue dots) are fitted to the function $\Omega_R = c\sqrt{P}$, where $k = 3.40(1)$ MHz/$\sqrt{\text{W}}$.

in SFig. 1a, the NV center can be treated as a pseudo-spin-1/2 system. The Hamiltonian of a continuous phase-modulated MW driving field on the NV center is given by:

$$H_S = \begin{pmatrix} 0 & \gamma_e B(t) cos\varphi(t) \\ \gamma_e B(t) cos\varphi(t) & D - \gamma_e B_0 \end{pmatrix} = \begin{pmatrix} 0 & \Omega(t) cos\varphi(t) \\ \Omega(t) cos\varphi(t) & f_1 \end{pmatrix}, \tag{7}$$

where $f_1 = D - \gamma_e B_0$, $\Omega(t) = \gamma_e B(t)$. After transforming the Hamiltonian to an appropriate rotating frame defined by the following unitary:

$$U_1 = \exp\left(-i \int_0^t H_1 dt'\right) = \begin{pmatrix} 1 & 0 \\ 0 & e^{-i\int_0^t g(t')dt'} \end{pmatrix} \tag{8}$$

and adopting the rotating-wave approximation, the Hamiltonian for the qubit is simplified to the standard form:

$$\begin{aligned} H_H &= U_1^\dagger H_S U_1 + i\left(\partial U_1^\dagger / \partial t\right) U_1 \\ &= \begin{pmatrix} 0 & 0 \\ 0 & f_1 - g(t) \end{pmatrix} + \frac{\Omega(t)}{2} \begin{pmatrix} 0 & e^{-i\left(\int_0^t g(t')dt' - \varphi(t)\right)} \\ e^{i\left(\int_0^t g(t')dt' - \varphi(t)\right)} & 0 \end{pmatrix}. \end{aligned} \tag{9}$$

If we set $g(t) = f_1$, $\int_0^t g(t')dt' - \varphi(t) = -\phi$, we will get the Hamilton of the Euler rotation:

$$H_{Euler} = \begin{pmatrix} 0 & \frac{\Omega}{2}e^{i\phi} \\ \frac{\Omega}{2}e^{-i\phi} & 0 \end{pmatrix} = \frac{\Omega}{2}\vec{n}_0 \cdot \vec{\sigma}.$$

Here, $\vec{n}_0 = (cos\phi, sin\phi, 0)$ and $\vec{\sigma} = (\sigma_x, \sigma_y, \sigma_z)$.

If we set $f_1 - g(t) = \Gamma(t)$, $\int_0^t g(t')dt' - \varphi(t) = 0$, we will get

$$H_H = \begin{pmatrix} 0 & 0 \\ 0 & \Gamma(t) \end{pmatrix} + \frac{\Omega(t)}{2}\begin{pmatrix} 0 & 1 \\ 1 & 0 \end{pmatrix}, \tag{10}$$

which is the same form of the Landau-Zener (LZ) Hamiltonian $H_{LZ} = \frac{\Gamma(t)}{2}\sigma_z + \frac{\Omega(t)}{2}\sigma_x$.

The sample rate of Keysight AWG is 12 GHz and the MW pulses generated by this function generator can be adjusted on the specific experimental sequence. The generated waveform is $s = a\cos\varphi(t)$ and the value of $\varphi(t)$ is given by $\varphi(t) = \int_0^t g(t')dt' = f_1 t - \int_0^t \Gamma(t')dt'$. For AF method, once the passage time τ is fixed, the average operation velocity is given by $\langle \mathrm{v}_z \rangle = \frac{are\cos\sqrt{F_0(\tau)}}{\tau}$. Since the operation velocity is in direct proportion to the amplitude $a(t)$ of MW, we have $\langle \mathrm{v}_z \rangle = \frac{K_1}{\tau}\int_0^\tau a(t')t' \leqslant \frac{K_1}{\tau}\int_0^\tau |a(t')|\, t'$, where K_1 is the proportionality coefficient. And energy cost for control field is $E_2 = K_2\int_0^\tau a(t')^2 t'$, where K_2 is another proportionality coefficient. By applying the inequality of arithmetic and geometric means, we have $E_2 = K_2\tau\frac{1}{\tau}\int_0^\tau a(t')^2 t' \geqslant \frac{K_2\tau}{K_1^2}\langle \mathrm{v}_z \rangle^2$. To reduce energy cost maximally, $a(t)$ must be a constant instead of a ramp-up and ramp-down shape.

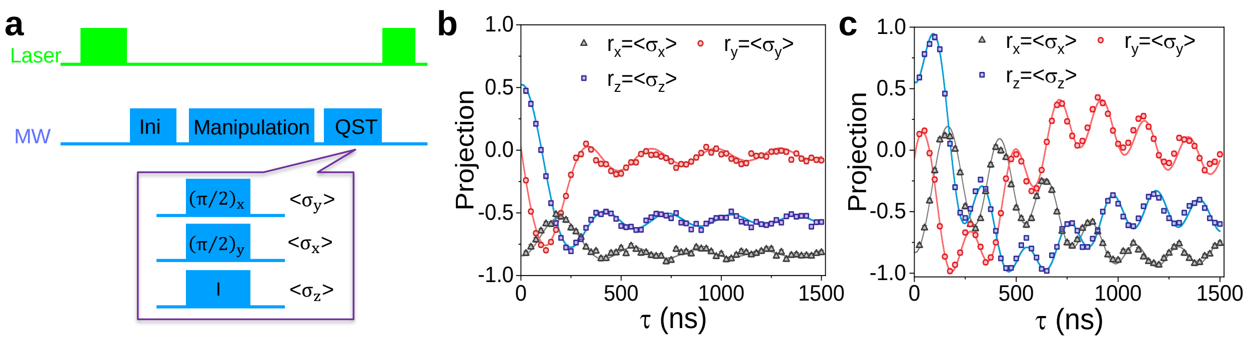

SFig. 3: **Quantum state tomography with NV center.** **a** Experimental pulse sequence for QST. Spin-state initialization and detection of the NV center are realized with a green laser. State trajectories under the H_{LZ} with different scan processes **b** $\Gamma_{linear} = 4\left(\frac{t}{\tau} - 0.5\right)$ MHz and **c** $\Gamma_{sin} = -4\left(\sin\left(\frac{3\pi}{2}\frac{t}{\tau}\right) + 0.5\right)$ MHz at $\Omega = 3$ MHz.

S4. Dynamics generated by the Landau-Zener Hamiltonian

SFig. 3a shows pulse sequences that are used to characterize the dynamic process of the LZ Hamiltonian. A green laser was applied in the beginning to initialize the electronic spin into $|0\rangle$ and at the end to readout the spin state. For fast linear scan field process like $\Gamma(t) = 16\left(\frac{t}{\tau} - 0.5\right)$ MHz with $\Omega \leqslant 2$ MHz, the overlaps between ground state $|0\rangle$ of NV center and the ground state $|g(0)\rangle$ of $H_{LZ} = \frac{\Gamma}{2}\sigma_z + \frac{\Omega}{2}\sigma_x$ is greater than 0.99. In this case, we initialize the NV center by a laser pulse into the state $|0\rangle$ and take it as $|g(0)\rangle$. However, for $\Gamma(t) = 4\left(\frac{t}{\tau} - 0.5\right)$ or $-4\left(\sin\left(\frac{3\pi}{2}\frac{t}{\tau}\right) + 0.5\right)$ MHz with $\Omega = 3$ MHz, the overlap between $|0\rangle$ and $|g(0)\rangle$ is not large enough and we implement a dynamic gate (i.e., an Euler rotation) to prepare $|g(0)\rangle$.The pulsed MW drives the LZ evolution. When doing quantum state tomography (QST), a series of different pulses, i.e., $(\pi/2)_x$, $(\pi/2)_y$, or the identity operator, are applied to the quantum system before readout. SFig 3b and 3c show the state $\rho(\tau)$ projections (r_x, r_y, r_z) under the H_{LZ} for two different scan processes Γ_{linear} and Γ_{sin}. For Γ_{linear} case, the quantum state is transfered into target state $|\psi_f\rangle$ with high fidelity $F = |\langle\psi_i'|\psi_f'\rangle|^2$ when the passenger time $\tau > 300$ ns. However, for Γ_{sin} case, the final quantum state change dramatically with the passenger time τ (as shown in SFig. 3c). For both scan field processes, the system can be driven from $|\psi_i\rangle$ to $|\psi_f\rangle$ with high fidelity for the large values of protocol time τ.

S5. Dynamics generated by the AF and STA methods

SFig. 4 shows instantaneous adiabaticity of the dynamics dictated by the AF method. The minimum adiabaticity of our method is observed at $\Omega = 0$ MHz, where the level crossing induces an exchange of roles between ground and excited states. In this limit, we get $\bar{A}_{\min} = \int_0^\tau A(\mathrm{t})dt \approx 0.82$ independently of the energy resource of the control [3]. The instantaneous adiabaticity $A(\mathrm{t})$ increases as the value of the energy gap increases. We found that for $\Omega = 2$ MHz, the resulting dynamics are adiabatic within an error less than 5%.

The fidelity of quantum state transfer at different passage time τ is shown in SFig. 5 for the AF and shortcuts to adiabaticity (STA) methods. In the case of the STA, we observe that as the system approaches the avoided crossing, the energy cost using the counterdiabatic (CD) field increases. This behavior can be explained using Fermi's golden rule for time-dependent perturbations, which states that the transition probabilities for the unperturbed problem are proportional to the time-integrated perturbation. Hence, if the relative magnitude of the perturbation is large, i.e., if the energy gap is small, transitions can be suppressed if the quantum system is prevented from lingering at the avoided crossing. When sufficiently far from the avoided crossing, the energy cost of the STA method [4] is largely independent of evolution time and in these regions, the instantaneous energy cost is close to zero. Approaching the avoided crossing requires that either the evolution is accordingly slowed down or a counterdiabatic field $H_{STA}(t)$ is used. Moreover, H_{STA} vanishes by construction in the beginning, $t = 0$, and the end, $t = \tau$, of the finite time process. For the LZ model with Γ_{linear}, H_{STA} takes the specific form [4]:

$$H_{STA} = -\frac{\Omega}{2} \frac{d\Gamma/dt}{\Gamma^2 + \Omega^2} \sigma_y. \tag{11}$$

Far away from the critical point the dynamics is essentially adiabatic. In the vicinity of the phase transition, the system response becomes sluggish, leading to the emergence of the impulse regime. In this regime, the system is more likely to undergo a transition the longer

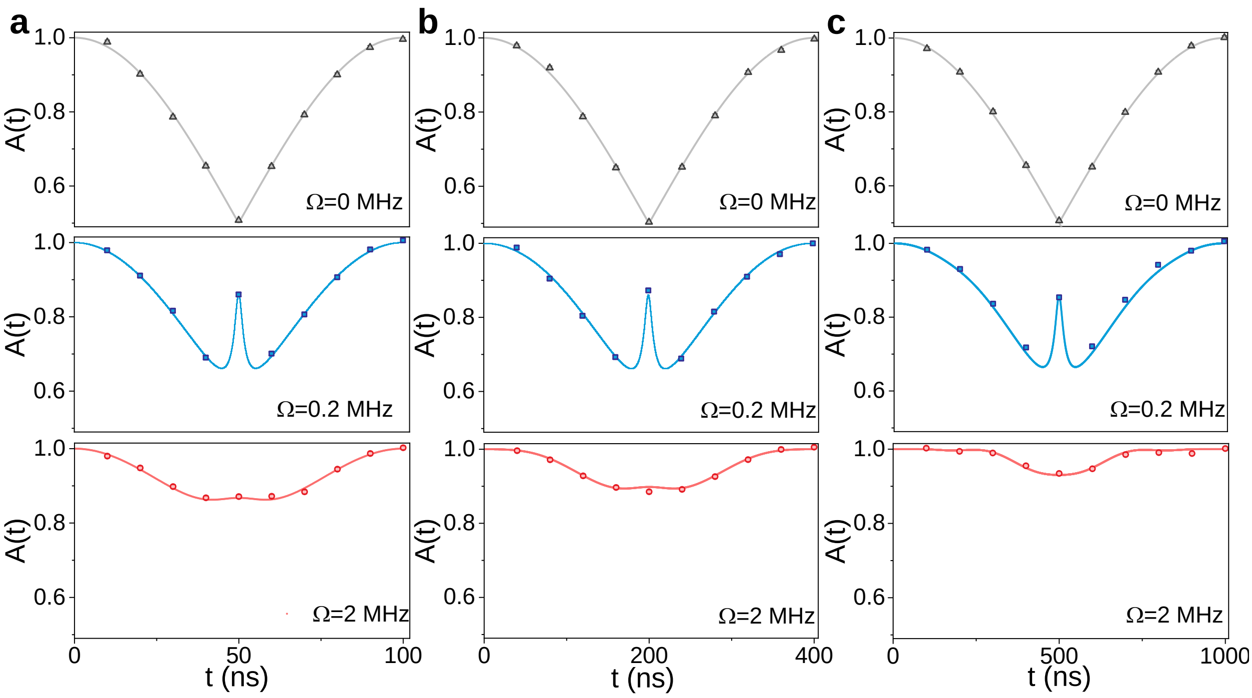

SFig. 4: **Experimental results of the instantaneous adiabaticity obtained with the implementation of the highly adiabatic time-optimal method for the LZ Hamiltonian.** The individual experiments correspond to $\Omega = 0$, 0.2, and 2 MHz for different values of the protocol time τ as shown in **a**-**c**. To measure those curves, we set $\Gamma_{linear} = 16\left(\frac{t}{\tau} - 0.5\right)$ MHz. The experimental data are shown as unfilled dots, and solid curves show the theoretical result for an ideal case.

it stays in it. However, suppressing excitations in the impulse regime requires a high energy cost. Therefore, the STA method aims to quickly bring the system back into the adiabatic regime, as shown in Fig. 2D, which is different from the AF method where the field strength associated with it remains relatively constant.

S6. Decay of Rabi oscillations in the Landau-Zener regime

We analyze the decay rate of Rabi oscillations under different MW field strength. We use two random fields along the σ_z and σ_x to simulate intrinsic and extrinsic noises [5], respectively. We assume that the local environment noise B_z is Gaussian distribution of zero mean value and variance of b^2, i.e., the distribution function is $P(B_z) = \frac{1}{b\sqrt{2\pi}} e^{\frac{-B_z^2}{2b^2}}$. The fluctuation is assumed to be independent of the microwave field. The fluctuation of the MW amplitudes is described by $\Delta' = \Delta(1+\varepsilon)$, where a Lorenztian distribution is adopted for ε [6], i.e., $P(\varepsilon) = \frac{1}{\pi}\frac{\gamma}{\gamma^2+\varepsilon^2}$, with γ the half width of the Lorentz distribution. In

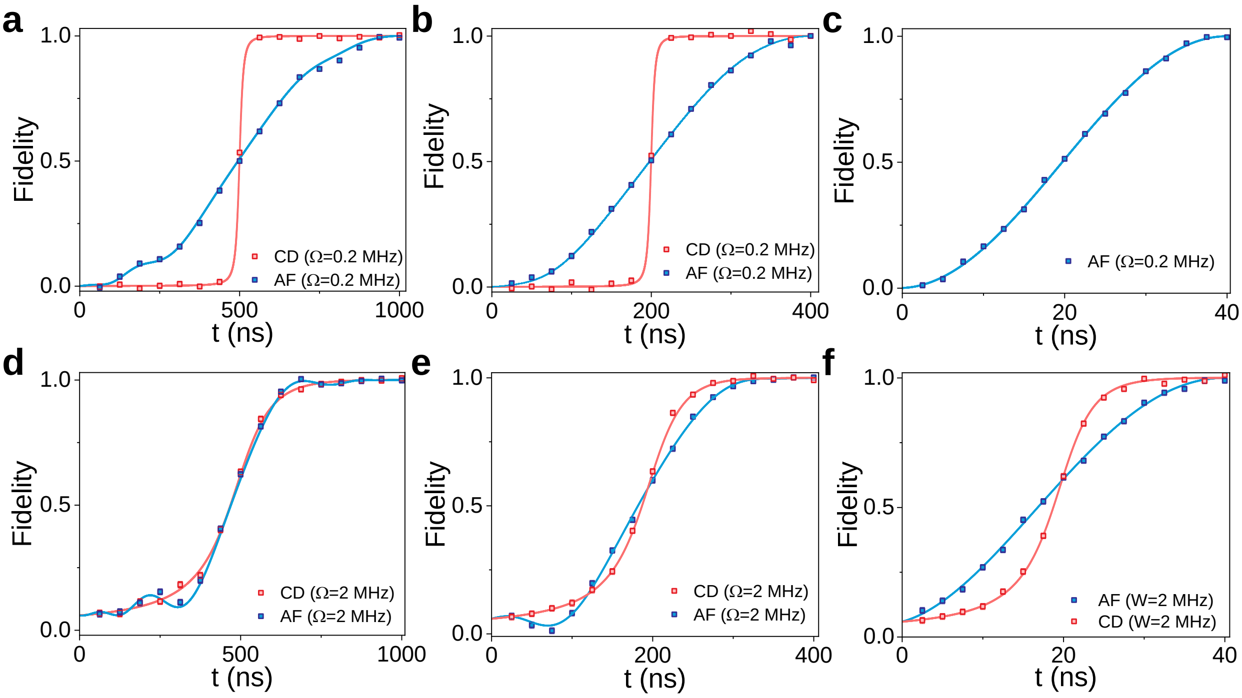

SFig. 5: **Quantum state transfer.** High fidelity quantum state transfer with different methods for $\Gamma = 16\left(\frac{t}{\tau} - 0.5\right)$ MHz. Experimental results obtained with the implementation of the AF and STA methods for the LZ Hamiltonian. The individual experiments correspond to the passenger time τ = 1000, 400 and 40 ns for different values of the energy gap Ω as shown in **a-f**. The experimental data are shown as unfilled dots. The solid blue curves show the theoretical result for an ideal AF method. The solid red curves show the theoretical result for an ideal STA method by adding a CD field.

the semiclassical picture, the Hamiltonian in the resonant fixed frequency Rabi oscillations (RFFRO) including the random component can be written in the rotation frame as follows:

$$\mathrm{H} = \frac{\mathrm{B_z}}{2}\sigma_{\mathrm{z}} + \frac{\Delta(1+\varepsilon)}{2}\sigma_{\mathrm{z}}$$

The static fluctuation of the energy δE can be approximately as:

$$\delta E \approx \frac{B_z^2}{2\Delta} + \varepsilon\Delta \tag{12}$$

The larger the value of δE, the faster the decay of the RFFOs. As the MW amplitude increases, the first term of Eq. (12) decreases while the second term increases. When the second term dominates, we obtain an increase in decay rate as the MW amplitude increases, similar to what is shown in Fig. 3 of the main text.

After transforming the Hamiltonian describing Landau-Zemer Rabi oscillations (LZRO) into rotating frame and neglecting non-resonant terms, we obtain the same Hamiltonian as that for RFFRO, except that Rabi frequency of RFFRO needs to be replaced with the Rabi frequency for the LZRO. When $\frac{b^2}{2\Delta_e} \ll \gamma\Delta_{\mathrm{e}}$, i.e. the fluctuation noise of MW field dominates, it can be shown that [5]:

$$\frac{\mathrm{T_{LZRO}}}{\mathrm{T_{RFFRO}}} = \frac{1}{|\ \mathrm{J_n}(\mathrm{A}/\omega)|}$$

where for the triangular scanning, $\mathrm{n} = 0$ and $\frac{\mathrm{A}}{\omega} = 4\,|\Gamma_0|\,\tau/\pi^3$ where Γ_0 is the absolute maximum value of the detuning. In our experiment $\Gamma_0 = 16\pi$ MHz and $\tau = 400$ ns. That yields $\frac{\mathrm{T_{LxRO}}}{\mathrm{T_{RFFRO}}} \approx 10$ (see SFig. 6). This value is in qualitative agreement to the measured ratio $\frac{\mathrm{T_{LZRO}}}{\mathrm{T_{RFFRO}}} \approx 4$.

S7. Cost analysis of arbitrary state preparation

We consider the energetic cost of preparing an arbitrary state of the form $|\psi_f\rangle = \cos\frac{\theta}{2}|0\rangle + e^{i\varphi}\sin\frac{\theta}{2}|1\rangle$. We systematically select 231 sets of (θ, φ), considering $|\psi_i\rangle = |0\rangle$. Taking $\Omega = 0.2$ MHz, $\Gamma = 16\left(\frac{t}{\tau} - 0.5\right)$ MHz, and $\tau = 40$ ns, we subsequently derive the corresponding 231 control Hamiltonians from Eq. (1) and implement the associated MW pulse sequences. Given a protocol time τ, the minimum energy required to bring an initial state $|\psi_i\rangle$ to a final state $|\psi_f\rangle$ is given by $\mathrm{v}_z = \frac{\arccos\sqrt{F_0}}{\tau}$, where $F_0 \equiv |\langle\psi_i'|\psi_f'\rangle|^2$ is the fidelity of the process dictated solely by H_{LZ}. In the absence of a drift Hamiltonian F_0 reduces to $|\langle\psi_i|\psi_f\rangle|^2$, yielding the well-known Mandelstam-Tamm (MT) bound, $\mathrm{v_{MT}} = \frac{\arccos\sqrt{|\langle\psi_i|\psi_f\rangle|^2}}{\tau}$. Note that the velocities v_z and $\mathrm{v_{AF}}$ are directly related with the energy cost of the operation through $E_2 = k_2\int_0^\tau \|H_c(t)\|^2 dt = k_2\tau v^2$. Therefore, in SFig. 7, we show the relative difference between v_z and $\mathrm{v_{AF}}$, i.e., $100\times\frac{\mathrm{v}_z{}^2-\mathrm{v_{MT}}{}^2}{|\mathrm{v}_{MT}{}^2|}$ as a function of the rotation angles (θ,φ). Approximately half of the qubit rotations were benefited by the quantum wind while the others showed a disadvantage. In each instance, the change in cost ranged from 0% to 50%, either decreasing or increasing relative to the cost associated to the Mandelstam-Tamm quantum speed limit.

S8. Robustness and energy cost of quantum gates

Systematic errors, such as amplitude ($\delta\mathrm{v}_z$) and detuning ($\delta\Gamma$) variations of the control fields, represent the primary sources of decoherence in the experiment. To deliberate on the robustness of the AF method, we have explored a wide range of $\delta\mathrm{v}_z$ and $\delta\Gamma$ values, entering the total Hamiltonian as follows $\mathrm{H_E} = \frac{\Gamma+\delta\Gamma}{2}\sigma_z + \frac{\Omega}{2}\sigma_\mathrm{x} + \frac{(\mathrm{v_z}+\delta\mathrm{v_z})}{\sqrt{1-\mathrm{s}^2}}\mathrm{U}_0\left(i\mathrm{e}^{-\mathrm{i}\beta}\,|\psi'_\mathrm{f}\rangle\,\langle\psi'_\mathrm{i}| + \mathrm{H.c.}\right)\mathrm{U}_0^\dagger$. As shown in SFig. 8, we find from experiments that the variations on the driving field strength and detunings have a similar impact on the fidelity.

To assess the energy efficiency of the AF method against a conventional approach employing Euler rotations, i.e., $R(\mathrm{z},\theta) = R(\mathrm{x},\pi/2)R(\mathrm{y},\theta)R(-\mathrm{x},\pi/2)$, we investigate the realization of a target rotation $R(\mathrm{z},\theta)$, where $\theta\in[0,\pi]$. With a fixed experimental gate duration of

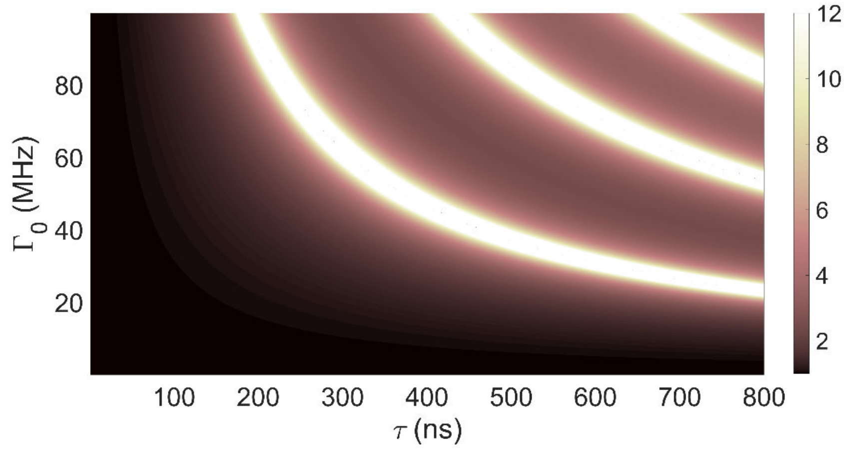

SFig. 6: **Coherence enhancement for AF method.** $\frac{\mathrm{T_{LZRO}}}{\mathrm{T_{RFFRO}}}$ as a function of the maximum value of the detuning Γ_0 and the protocol time τ for the triangular scanning defined in the main text. In our experiment $\Gamma_0 = 16\pi$ MHz and $\tau = 400$ ns. That yields $\frac{\mathrm{T_{LZRO}}}{\mathrm{T_{RFFRO}}}\approx 10$.

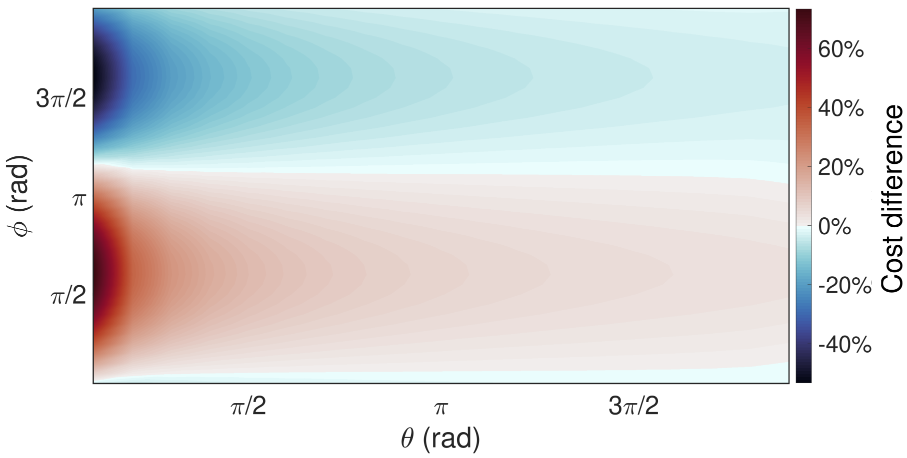

SFig. 7: **Cost analysis of arbitrary state preparation.** Relative difference between the energy resource of the AF control Hamiltonian, v_z, and the energy resource of the control in the absence of quantum wind, v_{MT}. Specifically, we plot $100 \times \frac{\mathrm{v}_z{}^2 - \mathrm{v}_{\mathrm{MT}}{}^2}{|\mathrm{v}_{MT}{}^2|}$ as a function of the rotation angles (θ, φ).

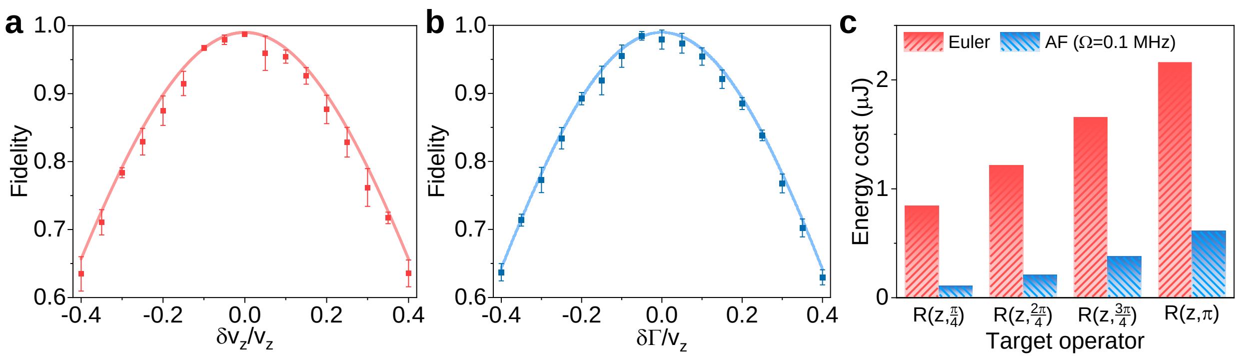

SFig. 8: **Robustness of AF method.** **a**, **b** Measured results and simulated fidelity of the X gate under various amplitude **a** and detuning fluctuations **b** of the control field for the AF method. The experimental parameters are $\Omega = 0.2$ MHz, $\Gamma = 16\left(\frac{\mathrm{t}}{\tau} - 0.5\right)$ MHz, and $\tau = 40$ ns. **c** Comparison of quantum gate energy costs for different rotation along the z-axis.

$\tau = 40$ ns, the comparison of energy costs E_2 for gate operations between the AF method and Euler rotations is illustrated in SFig. 8c. Significantly, the energy expenditure associated with the AF method is notably lower than that of Euler rotations across all rotation angles. Particularly noteworthy is the implementation of the non-Clifford gate $T = R(\mathrm{z}, \pi/4)$ using the AF method, which consumes only 12.7% of the energy required by Euler rotations.

---

* Electronic address: fwsun@ustc.edu.cn; guillealpi@gmail.com

[1] Dong, Y., Zhang, S.-C., Lin, H.-B., Chen, X.-D., Zhu, W., Wang, G.-Z., Guo, G.-C. & Sun, F.-W. Quantifying the performance of multipulse quantum sensing. *Phys. Rev. B* **103**, 104104 (2021).

[2] Dong, Y., Feng, C., Zheng, Y., Chen, X.-D., Guo, G.-C. & Sun, F.-W. Fast high-fidelity geometric quantum control with quantum brachistochrones. *Phys. Rev. Research* **3**, 043177 (2021).

[3] Garcia, L., Bofill, J. M., de PR Moreira, I. & Albareda, G. Highly adiabatic time-optimal quantum driving at low energy cost. *Phys. Rev. Lett.* **129**, 180402 (2022).

[4] Guéry-Odelin, D., Ruschhaupt, A., Kiely, A., Torrontegui, E., Martínez-Garaot, S. & Muga, J. G. Shortcuts to adiabaticity: Concepts, methods, and applications. *Rev. Mod. Phys.* **91**, 045001 (2019).

[5] Zhou, J., Huang, P., Zhang, Q., Wang, Z., Tan, T., Xu, X., Shi, F., Rong, X., Ashhab, S. & Du, J. Observation of time-domain Rabi oscillations in the Landau-Zener regime with a single electronic spin. *Phys. Rev. Lett.* **112**, 010503 (2014).

[6] De Raedt, H., Barbara, B., Miyashita, S., Michielsen, K., Bertaina, S. & Gambarelli, S. Quantum simulations and experiments on Rabi oscillations of spin qubits: Intrinsic vs extrinsic damping. *Phys. Rev. B* **85**, 014408 (2012).